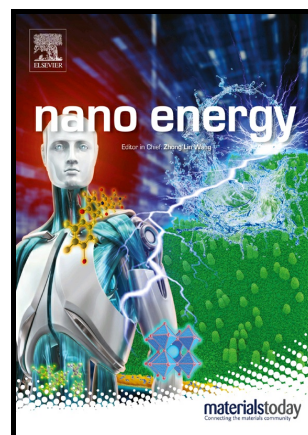


Deciphering Interpenetrated Interface of Transition Metal Oxides/Phosphates from Atomic level for Reliable Li/S Electrocatalytic Behavior

Daorui Wang, Dan Luo, Yongguang Zhang, Yan Zhao, Guofu Zhou, Lingling Shui, Zhongwei Chen, Xin Wang



PII: S2211-2855(20)31175-7

DOI: <https://doi.org/10.1016/j.nanoen.2020.105602>

Reference: NANOEN105602

To appear in: *Nano Energy*

Received date: 30 September 2020

Revised date: 8 November 2020

Accepted date: 9 November 2020

Please cite this article as: Daorui Wang, Dan Luo, Yongguang Zhang, Yan Zhao, Guofu Zhou, Lingling Shui, Zhongwei Chen and Xin Wang, Deciphering Interpenetrated Interface of Transition Metal Oxides/Phosphates from Atomic level for Reliable Li/S Electrocatalytic Behavior, *Nano Energy*, (2020) doi:<https://doi.org/10.1016/j.nanoen.2020.105602>

This is a PDF file of an article that has undergone enhancements after acceptance, such as the addition of a cover page and metadata, and formatting for readability, but it is not yet the definitive version of record. This version will undergo additional copyediting, typesetting and review before it is published in its final form, but we are providing this version to give early visibility of the article. Please note that, during the production process, errors may be discovered which could affect the content, and all legal disclaimers that apply to the journal pertain.

© 2020 Published by Elsevier.

Deciphering Interpenetrated Interface of Transition Metal Oxides/Phosphates from Atomic level for Reliable Li/S Electrocatalytic Behavior

Daorui Wang^{a1}, Dan Luo^{d1}, Yongguang Zhang^{a,b*}, Yan Zhao^b, Guofu Zhou^c, Lingling Shui^a, Zhongwei Chen^{d*}, Xin Wang^{a,c*}

^a School of Information and Optoelectronic Science and Engineering & International Academy of Optoelectronics at Zhaoqing, South China Normal University, Guangzhou 510006, China

^b School of Materials Science and Engineering, Hebei University of Technology, Tianjin 300130, China

^c South China Academy of Advanced Optoelectronics, South China Normal University, Guangdong 510006, China

^d Department of Chemical Engineering, University of Waterloo, Waterloo, ON, Canada N2L 3G1

*Corresponding author:

Email: yongguangzhang@hebut.edu.cn (Y. Zhang); wangxin@scnu.edu.cn (X. Wang); zhwchen@uwaterloo.ca (Z. Chen)

¹The authors contributed equally to this work

Abstract

Lithium/sulfur (Li/S) batteries have superior advantages in their high energy-density and environmental benignity. However, the notorious shuttle effect of lithium polysulfides (LiPSs) and their sluggish redox reaction kinetics hinder their practical implementation. Herein, a electronic modulation strategy was developed to regulate the catalytic behavior of transition metal oxides (TMOs)/transition metal phosphates (TMPs) interface towards Li/S surface chemistry. Thus, the reduced energy gap between the energy centers of the cation 3d and anion 2p band in O-M-P

bridging (M refers to the transition elements) effectively reduce the energy barrier of LiPSs conversion and improve the electron transfer owing to the interdoping effect, which further functions as catalytic centers to active the M sites for regulating LiPSs adsorption-diffusion-conversion process. Benefited from these structural advantages, the engineered TMOs/TMPs exhibits admirable electrocatalytic sulfur reaction kinetics based on theoretical calculations and electrochemical analyzations. As expected, the TMOs/TMPs sulfur cathode exhibits an ultralow capacity fading rate of 0.033% per cycle at 1 C over 500 cycles. Even under raising sulfur loadings and lean electrolyte content, this cathode still exhibits outstanding electrochemical performance.

Keywords: interpenetrated interface; electronic modulation; polysulfides; lithium/sulfur batteries; catalytic behavior

1. Introduction

Lithium/sulfur (Li/S) batteries are widely accepted as the next generation rechargeable energy storage systems benefiting from its high specific energy density (2600 Wh kg⁻¹), cost-effective, as well as the natural abundance and nontoxicity of sulfur. [1-4] Yet, several challenges still hamper the practical utilization of Li/S batteries, which involve the electronic insulating of sulfur/Li₂S, almost 80% volume expansion upon cycling, the shuttling behavior of lithium polysulfides (LiPSs) intermediate and the sluggish reaction kinetics. Under this circumstance, the Li/S batteries suffer from huge active materials loss, poor rate capability and cyclic stability, rendering unsatisfied electrochemical performance.[5-8]

To deal with these conundrums, strategies are concentrated on solving the above-mentioned bottlenecks by developing advanced sulfur cathode. Excellent sulfur host materials are in urgent need for immobilizing LiPSs and accelerating sulfur redox reactions. Carbonaceous materials, such as porous carbon,[9-12] carbon spheres,[13] carbon nanotubes,[14, 15] and graphene[16] have been quite extensively applied as the sulfur cathode to inhibit LiPSs shuttle behavior and promote the cyclability. However, the adsorption of LiPSs on the carbonaceous materials sulfur hosts are dependent on the physical interaction, van der Waals force, which are insufficient to adsorb and inhibit the shuttle effect of LiPSs.[17-19] To further promote the battery performance, various polar host materials with strong LiPSs chemisorption are developed. Among them, transition metal compounds (TMCs) have been extensively studied as sulfur stockpile owing to their capability of tailoring electronic structure,[20] which have been demonstrated to be able to adjust the d-band center of metal sites to regulate adsorption-desorption behaviors for LiPSs adsorbates. The manipulation of energy gap between d orbitals of transition metal centers and non-metal anions p orbitals in TMCs also affects electronic concentration in the Fermi level,[21] which has substantial impact on bonding and breaking of LiPSs adsorbate. Consequently, the electronic structure of TMCs can be feasibly modulated by regulating electronic structure, endowing TMCs with optimized LiPSs adsorption and decent electrocatalytic conversion capability. Among them, transition metal oxides (TMOs) present much stronger adsorption of LiPSs compared with the other materials, resulting from their larger polar surface through formation of the oxygen-lithium

binding. However, the intrinsic low conductivity, limited specific surface area and insufficient active sites of most TMOs render unsatisfied Li/S batteries performance. Meanwhile, transition metal phosphides (TMPs) exhibits metallic conductivity in contrast to most metal oxides and sulfides[22] as well as high catalytic activity for LiPSs conversion. However, their LiPSs adsorption capacity is much lower than that of metal oxides, which greatly impedes their widespread implementation. Under this circumstances, constructing heterostructure is effective way to synergy with each other's advantages for Li/S batteries application. For instance, Zhou *et al.* designed a twinborn TiO₂/TiN heterostructured material loaded onto graphene substrate, which could strongly trap and accelerate LiPSs conversion, as well as improve sulfur utilization.[23] Liu *etal.* reviewed the merits of heterostructure to meet ultralong life Li/S battery.[24] Therefore, it is of far-reaching significance to design heterostructured materials to offset TMOs and TMPs shortcomings. However, the most of the studies base on heterojunction system are focused on experimental phenomena. Although few studies have been adjusted energy band centres to develop sulfur cathode host, their work focus on d modulation based on single phase material. [25, 26] More importantly, the relationship between cation 3d and anion 2p band affect the Li/S catalytic process on heterogeneous interface is still lacking. Therefore, by combing polar TMOs materials' features with the merits of TMPs to construct the O-M-P (M refers to transition metal elements) interpenetrated interface will be an effective strategy to offset the deficiency. The highly electronegative O can activate high-valence M sites and thus chemically bonding LiPSs to form M-S bonding and

leave Li-O-P moieties on the O-M-P surface. Additionally, the interpenetration of O-M-P could further improve the conductivity and electron transfer of TMOs or TMPs, which may lead to the simultaneous enhancement of Li_2S deposition and promoted LiPSs catalytic conversion. These superiorities of TMOs/TMPs materials may boost LiPSs catalytic conversion from atomic level, which can further guide materials design towards accelerated Li/S electrochemistry.

However, an intractable challenge is that TMOs/TMPs heterostructured materials usually demonstrate poor ionic/electronic conductivity, limited specific surface area and insufficient active sites, which blocks mass/charge transfer and impedes ion/electron transportation, leading to sluggish redox reaction kinetics of Li/S batteries. In this case, designing multi-dimensional nanoarchitecture sulfur immobilizer is able to provide better electron and ion transportation of reaction-relevant species to the electrocatalyst. Among different materials, three dimensional ordered mesoporous (3DOM) structure offers abundant active surface area and establishes interconnected channels for favored ion diffusion of electroactive species, which can facilitate charge/mass transfer process towards expedited redox reactions.

Herein, a simple and efficient method for synthesizing 3DOM TMOs/TMPs nanospheres with interpenetrated interface was developed to reveal excellent Li/S performance. The fast LiPSs electrocatalytic effect on the heterointerface was further illuminated by density functional theory (DFT) calculations. The 3DOM TMOs/TMPs heterostructured material presented excellent electrochemical performance benefiting

from its structure advantages: 1) the interconnected mesoporous framework promotes electrolyte infiltration and apparently immobilizes the sulfur species; 2) TMOs provides strong chemical adsorption of LiPSs, which further suppresses the LiPSs shuttle effect; 3) TMPs highly accelerates the catalytic conversion of LiPSs for fast redox reaction; 4) the reduced energy gap between the energy centers of the cation 3d and anion 2p bands center facilitates LiPSs diffusion and decomposition on the heterointerface, leading to promoted LiPSs transformation. Attributed to these structural superiorities, the as-fabricated 3DOM Co₃O₄/CoP sulfur composites exhibit promoted sulfur utilization, intriguing cycling stability, and superb rate capability, even under raised sulfur loading and lean electrolyte/sulfur (E/S) ratio. Accordingly, this sulfur immobilizer design strategy offers promising vision on the development of Li/S batteries, which also lays a foundation for electrode design in other related electrochemical applications.

2. Experimental

2.1 Synthesis of 3DOM Co₃O₄ nanospheres

The silica nanospheres sols with the size ca. 30 nm were prepared by a Stöber method according to the previous work.[27] The resulting sols were further self-assembled into the 3DOM array as a template under room temperature. 1 g Co(NO₃)₂·6H₂O was dispersed in 10 mL ethanol containing 0.5 g of the above prepared silica nanospheres, which was stirred at 75 °C until the solution was dried. The resultant composites were calcined at 600 °C in the air at 1 °C min⁻¹ for 6 h. And the containing silica template was etching from the obtained powder by 2 M NaOH

solution, followed by washing several times, and thus obtained the 3DOM Co_3O_4 nanospheres.

2.2 Synthesis of the 3DOM $\text{Co}_3\text{O}_4/\text{CoP}$ heterostructure nanospheres

0.2 g 3DOM Co_3O_4 nanospheres and 2 g $\text{NaH}_2\text{PO}_2 \cdot \text{H}_2\text{O}$ were mixed together and grinded to a fine powder, followed by heating at 300 °C for 30 min under Ar. The final product was washed several times with deionized water and denoted as 3DOM $\text{Co}_3\text{O}_4/\text{CoP}$. The same procedure was performed to prepare 3DOM CoP nanospheres except for the annealing time controlled at 2 h.

2.3 Synthesis of S- $\text{Co}_3\text{O}_4/\text{CoP}$ heterostructure nanospheres composites

S- $\text{Co}_3\text{O}_4/\text{CoP}$ composites were synthesized by melt-diffusion method, in which sulfur powder and 3DOM $\text{Co}_3\text{O}_4/\text{CoP}$ nanospheres with a mass ratio of 3:1 were ground well and heated in a bottle at 155 °C for 6 h under Ar atmosphere.

2.4 Material characterization

X-ray diffractometer (XRD) data were acquired on a Bruker D8 Advance XRD to determine the crystal structure of the samples with $\text{Cu K}\alpha$ radiation. Scanning electron microscopy (SEM, Hitachi S-4800) and transmission electron microscopy (TEM, JEOL 2100) were operated to characterize the morphology of the samples. The Brunauer-Emmett-Teller (BET) was measured on a nitrogen adsorption/desorption test (Quantachrome Instruments, Autosorb AS-6B). X-ray photoelectron spectroscopy (XPS, Thermo SCIENTIFICESCALAB250Xi) was recorded to analysis the chemical bonds, and calibrated all binding energy by C 1s at 284.8 eV. Thermal gravimetric analysis (TGA, TA Instruments, SDT Q-600) was carried out under Ar

atmosphere. The UV-vis spectra were acquired at 200-600 nm spectral range on a Cary 60 UV-vis spectrophotometer. Synchrotron X-ray Diffraction were performed at Canadian Light Source Inc, Canada, using the BioXAS-side (07ID-2) beamlines.

2.5 Electrochemical characterizations

The slurry was prepared by mixing 70% 3DOM $\text{Co}_3\text{O}_4/\text{CoP}$, 10% PVDF binder and 20% Super-P with 1-methyl-2-pyrrolidinone (NMP). The mixture was then cast on carbon-coated aluminum foil and dried at 60 °C overnight. The electrolyte was prepared containing 1.0 M LiTFSI with 1% LiNO_3 as an additive and further dissolved in a 1:1 vol ratio of DOL and DME. CR2032 coin cells were assembled with S cathodes, electrolyte, polypropylene separators (Celgard 2400) and lithium foils in argon-filled glove-box. The sulfur loading was ca. 1.4 mg cm^{-2} . The cycling performance and rate measurement were performed via Neware (Shenzhen, China) tester system with a voltage range from 1.7 to 2.8 V (vs. Li^+/Li). Bio-Logic VMP3 electrochemical workstation was carried out to perform cyclic voltammetry (CV) with a scan rate of 0.1 mV s^{-1} from 1.7 to 2.8 V (vs. Li^+/Li).

2.6 Computational method

The DFT calculations were performed using Perdew-Burke-Ernzerhof (PBE) to calculate electron exchange-correlation interactions. A 2×1 supercell and Monkhorst-Pack with $(2 \times 2 \times 1)$ k-point integrates the Brillouin zones. The vacuum height of 15 Å and energy cutoff of 400 eV were used. Geometry optimizations were performed at 0.02 eV/Å for the stress convergence and energy convergence within 10^{-5} eV. The P- Co_3O_4 , Co_3O_4 (311) and O-CoP, CoP (211) surfaces were chosen to

investigate the interaction with Li_2S_6 . The adsorption energy (ΔE_{ads}) was expressed by the following equation:

$$\Delta E_{\text{ads}} = E_{\text{ads/base}} - E_{\text{ads}} - E_{\text{base}}$$

where $E_{\text{ads/base}}$, E_{ads} and E_{base} are the total energy of the adsorbed surface, Li_2S_6 specie, and the model, respectively.

2.7 Preparation of Li_2S_6 electrolyte

Li_2S and sulfur (1:5 in molar ratio) were dissolved in DOL/DME (v/v = 1/1), and stirred in the Ar-filled glove box 24 h to get 0.2 M Li_2S_6 electrolyte for symmetric cells assembly. In addition, 5 mM Li_2S_6 electrolyte for the adsorption test was prepared by the same method.

2.8 Symmetric cells assembly and measurement

The active materials were dispersed in ethanol and then drop-casted onto the circular disks carbon papers (12 mm in diameter), and the mass loading was controlled to be 0.5 mg cm^{-2} . Meanwhile, 25 μL 0.2 M Li_2S_6 electrolyte was added to assemble Li_2S_6 symmetric cells. The CV curves were measured between -1.5 and 1.5 V at 6 mV s^{-1} . The electrochemical impedance spectroscopy (EIS) also recorded on the VMP3 electrochemistry system.

2.9 Linear sweep voltammetry (LSV) measurement

LSV curves were used to evaluate Li_2S oxidization activity of 3DOM $\text{Co}_3\text{O}_4/\text{CoP}$ composites in 0.1 M Li_2S /methanol electrolyte via three-electrode system under ambient temperature. The cells consisted of a working electrode (glass carbon), a reference (Ag/AgCl electrode), and a counter electrode (platinum wire). Specifically,

the 3DOM Co₃O₄/CoP composites were dispersed in NMP, and then the obtained slurry was coated on the glass carbon electrode as the working electrode. The mass loading of 3DOM Co₃O₄/CoP on the working electrode was kept around 0.5 mg cm⁻². For comparison, the Co₃O₄ and CoP working electrodes were modified respectively by the same process. The LSV measurements were conducted at 5 mV s⁻¹ from -0.8 to -0.1 V (Vs. Ag/AgCl).

2.10 Li₂S deposition measurement

0.25 M Li₂S₈ electrolyte was prepared in a similar way to the Li₂S₆ electrolyte, except that the solvent was tetraglyme. During the preparation process, 3DOM Co₃O₄/CoP composites, lithium foil, and Celgard 2400 were used as the current collector for cathode, anode, and separator, respectively. 20 μL Li₂S₈ electrolyte was dropped onto 3DOM Co₃O₄/CoP composites cathode, while 20 μL blank electrolyte without Li₂S₈ was dropped onto the lithium anode side by pipette, respectively. For comparison, the 3DOM Co₃O₄ and 3DOM CoP cells were prepared by the same process. The cells were galvanostatically discharged at 0.112 mA to 2.06 V followed by keeping potentiostatically at 2.05 V, until the current decreased to 10⁻⁵ A.

3. Results and Discussion

In order to illustrate the fast adsorption-diffusion-conversion of LiPSs on TMOs/TMPs, DFT calculations were used to reveal its electronic structure and illuminate the underlying mechanism of enhanced catalytic effect of heterostructured materials. Co₃O₄ and CoP were selected as representative materials to investigate the modulation of electronic structure by constructing interpenetrated interface, which

was simulated by using O-CoP and P-Co₃O₄ as model. The formation of heterointerfaces weaken the hybridization interaction between Co 3d orbital and anion 2p orbital and thereby result in narrowed d-band of Co sites, which in turn beneficially regulate the adsorption behaviors. Besides, the highly electronegative O induce high-valence Co sites to bond with LiPSs by forming Co-S bonding, leading to increased LiPS interaction on the interface. Besides, the interpenetration of O-Co-P interface with different band gaps could induce internal electric field to improve ion/electron diffusion, increase the electrochemical active sites and reaction dynamics process, thus facilitating LiPSs catalytic conversion. The d band manipulation further alters the chemical interaction between LiPSs and TMOs/TMPs heterostructured material towards desirable LiPSs adsorption capability. Compared with TMOs and TMOs, TMOs/TMPs heterojunction demonstrates an upshifted d band center, thereby weakening the S-S bonds and emptying antibonding orbitals probably, giving rise to the strong adsorption of LiPSs. The density of states (DOS) calculation results indicate that CoP exhibits better electronic conductivity than that of Co₃O₄, since more peaks appear around the Fermi level (Fig. S1, Supporting Information). After engineering heterointerfaces, the states of P-Co₃O₄ and O-CoP cross the Fermi energy (Fig. S1), indicating 3DOM Co₃O₄/CoP still retains the metallic nature, rendering facilitated charge transfer process. The partial density of states (PDOS) of the anion 2p band and cation 3d band (Fig. 1a) display the reduced energy gap between bonding and antibonding orbitals of P-Co₃O₄ (1.89 eV) and O-CoP (1.57 eV) compared with corresponding Co₃O₄ (1.96 eV) and CoP (2.18 eV), respectively. The reduced energy

gap values cause the non-metal atoms easily bonding with other atoms to achieve a higher electronic concentration at Fermi level, and thus expedite the electron exchange for S_6^{2-}/S^{2-} transformation, rendering accelerated LiPSs conversion. Therefore, modulating p and d band positions of TMOs/TMPs heterointerfaces could offer valuable views for Li/S batteries chemistry. Also, the method of adjusting energy band position of TMOs/TMPs we proposed here can general design low-barrier catalysts to understand the LiPSs conversion at the atomic level, including introduced heterogeneous elements, selectively exposed surface, defect engineering, and heterostructure construction.

The superb adsorption energy of Li_2S_6 on O-CoP and P- Co_3O_4 compared with counterpart CoP and Co_3O_4 indicates a favorable adsorption-desorption process for fast redox reaction. Fig. 1b presents the optimized geometries adsorption profile of Li_2S_6 on Co_3O_4 , CoP, P- Co_3O_4 and O-CoP surfaces. P- Co_3O_4 and O-CoP surfaces with abundant localized electrons can serve as active centers for the adsorption polysulfide and facilitate the S-S bond breaking of LiPSs, rendering reduced the activation barrier. As a result, the adsorption energy of Li_2S_6 on Co_3O_4 (311), CoP (211), P- Co_3O_4 (311) and O-CoP (211) surfaces is -3.17, -2.13, -3.40 and -2.77 eV, respectively. Meanwhile, the charge transport is improved by manipulating the band structure and regulating the valence band by P and O elements as well as the strong electron trapping ability of P- Co_3O_4 and O-CoP surfaces caused by the redistributed electron population. Thus, the Co_3O_4 /CoP heterostructured material delivers the lower Li_2S decomposition energy barrier of O-CoP (0.66 eV) and P- Co_3O_4 (0.97 eV), much

lower than that of Co_3O_4 (1.03 eV) and CoP (0.74 eV) respectively, indicating its hastened LiPSs catalytic conversion capability (Fig. 1c). The fast LiPSs conversion process on $\text{Co}_3\text{O}_4/\text{CoP}$ heterostructured material was further evaluated by analyzing Li^+ diffusion energy barrier. Fig. 1d shows the Li^+ diffusion energy barrier based on Co_3O_4 (311), P- Co_3O_4 (311) and CoP (211), O-CoP (211) surface. Clearly, O-CoP and P- Co_3O_4 show the lower Li^+ diffusion energy barrier (0.17, 0.33 eV, respectively) than corresponding CoP (0.23 eV) and Co_3O_4 (0.35 eV), demonstrating the enhanced catalytic kinetics of $\text{Co}_3\text{O}_4/\text{CoP}$ heterointerfaces. Inspired by the above calculations, we can infer that the TMOs serve as the adsorption centers to capture LiPSs and transfer to the higher conductivity of TMPs for Li_2S nucleation. Therefore, it is theoretically feasible to regulate electronic state by designing TMOs/TMPs heterostructured material toward superior LiPSs catalytic performance.

As for demonstration, the 3DOM TMOs/TMPs heterostructured material was synthesized as multifunctional sulfur immobilizer. The rapid LiPSs adsorption-diffusion-conversion process on the TMOs/TMPs heterointerface was well illustrated in Fig. 2. Briefly, the formed 3DOM TMOs/TMPs not only acts as sulfur reservoir and physical buffer, but also inherits the merits of polar TMOs with high adsorption energy to mitigate the shuttle effect of LiPSs effectively, and the strong catalytic activity capacity of TMPs for solid Li_2S nucleation/conversion. Meanwhile, the heterogeneous interface could induce an internal electric field that accelerates electron transfer,[28-30] guaranteeing the smooth diffusion of LiPSs from TMOs to TMPs for the further catalytic conversion. With the synergistic effect between TMOs

and TMPs, the S-TMOs/TMPs composites could display excellent electrochemical performance.

Specifically, the synthetic process of 3DOM $\text{Co}_3\text{O}_4/\text{CoP}$ heterostructured material was schematically illustrated in Fig. S2. Firstly, the monodispersed SiO_2 array is synthesized via the sol-gel method. Next, $\text{Co}(\text{NO}_3)_2$ is deposited into the void space of the silica opal via capillary force, and thus the 3DOM Co_3O_4 nanospheres are achieved after calcination and followed by removing the SiO_2 template. Finally, the 3DOM $\text{Co}_3\text{O}_4/\text{CoP}$ heterostructured material is achieved by the reducibility of PH_3 gas, which is generated by the decomposition of the $\text{NaH}_2\text{PO}_2 \cdot \text{H}_2\text{O}$.

The morphology of synthesized materials was recorded by SEM. The 3DOM Co_3O_4 nanospheres present an average diameter of 400 nm in the large scale (Fig. S3a), and the 3DOM $\text{Co}_3\text{O}_4/\text{CoP}$ could keep well structural stability after phosphating for 30 min (Fig. 3a, b), and the histograms of 3DOM $\text{Co}_3\text{O}_4/\text{CoP}$ nanospheres in the inset of Fig. 3a also present well defined spherical size centred at 400 nm, which is beneficial to expose abundant active sites. The corresponding elemental mapping shows that Co, P and O are evenly distributed on the spherical 3DOM $\text{Co}_3\text{O}_4/\text{CoP}$ (Fig. 3c). However, the seriously collapsed and aggregated structure of 3DOM CoP nanospheres was observed under a harsh PH_3 atmosphere for 2 h (Fig. S3b). Furthermore, the elements Co, O, P, S are evenly dispersed in the whole S- $\text{Co}_3\text{O}_4/\text{CoP}$ composite (Fig. S4), indicating the uniform distribution of sulfur on 3DOM $\text{Co}_3\text{O}_4/\text{CoP}$ heterostructured material. The 3DOM $\text{Co}_3\text{O}_4/\text{CoP}$ TEM image (Fig. 3d) also reveals its ordered mesoporous nanostructure. Fig. 3e presents the higher

magnification image of the 3DOM $\text{Co}_3\text{O}_4/\text{CoP}$ nanospheres, which exhibits the ordered mesoporous structure with a pore diameter of 20 nm. The corresponding selected area electron diffraction pattern of the 3DOM $\text{Co}_3\text{O}_4/\text{CoP}$ nanospheres (Fig. 3f) exhibits several ring-like diffraction patterns, indicating the formation of polycrystalline Co_3O_4 and CoP. The formation of such a porous structure could provide a large accessible surface area for mass transport and allow the molten sulfur readily penetrating into the host, and thus homogenizing sulfur distribution and improving electrochemical performance. The clear heterostructured interface between Co_3O_4 and CoP is revealed by HRTEM in Fig. 3g, which plays the dynamic reaction sites to adsorb LiPSs as well as accelerates electron transformation during LiPSs conversion.[31-33] The interplanar distance of the interface is ca. 0.243 nm in the red region, which can be assigned to the (311) lattice plane of Co_3O_4 , whereas the characteristic d-spacing ca. 0.189 nm in the blue region, corresponding to CoP (211) plane (Fig. 3h). The elemental mapping (Fig. S5) reveals a uniform element distribution of Co, P, and O of the 3DOM $\text{Co}_3\text{O}_4/\text{CoP}$. Overall, this 3DOM $\text{Co}_3\text{O}_4/\text{CoP}$ offers large void space and large surface area to uniform sulfur distribution and provides spatial confinement to block LiPSs migration, leading to enhanced sulfur reservation.

The structure information of the 3DOM $\text{Co}_3\text{O}_4/\text{CoP}$ is further obtained by XRD analysis in Fig. 4a. Co_3O_4 sample displays the typical diffraction peaks of cubic Co_3O_4 (JCPDS 74-2120). In the 3DOM $\text{Co}_3\text{O}_4/\text{CoP}$, an extra peak appears around 48.1° , which can be ascribed to the (211) diffraction peak of the CoP (JCPDS 89-2747),

indicating the existence of the CoP. By increasing the phosphorization calcination time to 2 h, only CoP diffraction peak can be observed, corresponding to the complete transformation from Co_3O_4 to CoP. Fig. 4b shows the N_2 adsorption-desorption isotherms of the 3DOM $\text{Co}_3\text{O}_4/\text{CoP}$ nanospheres. Obvious IV isotherms with the H3 hysteresis loop in the 3DOM $\text{Co}_3\text{O}_4/\text{CoP}$ nanospheres corroborates the existence of the mesoporous structure. The specific surface area and pore volume of the 3DOM $\text{Co}_3\text{O}_4/\text{CoP}$ nanospheres are determined to be $65.5 \text{ m}^2 \text{ g}^{-1}$ and $0.75 \text{ cm}^3 \text{ g}^{-1}$, respectively. Pore size distribution (PSD) is calculated by the Barrett-Joyner-Halenda method in Fig. 4c, indicating the mesoporous feature of the 3DOM $\text{Co}_3\text{O}_4/\text{CoP}$. The sufficient surface area and large pore volume could serve as the reservoir, which facilitates the deposition of insulating $\text{Li}_2\text{S}_2/\text{Li}_2\text{S}$ and accommodates the volume expansion during sulfur lithiation, leading to enhanced structure stability. The XPS spectra are further conducted to verify the valence state. Fig. S6 shows the presence of P, O and Co elements, in which the surface concentration of phosphorus is ca.14%. The peaks located at the binding energy of 779.8 and 781.1 eV (Fig. 4d) can be ascribed to the Co^{3+} species and Co^{2+} species in Co_3O_4 , respectively.[34] After phosphorization, a Co-P peak located at 778.7 eV can be observed,[35] indicating the phase transition from Co_3O_4 to CoP. The CoP phase is further confirmed according to the P-O bond (133.2 eV) in the P 2p spectrum (Fig. 4e), and the other peaks at 129.3 and 130.2 eV are assigned to P $2p_{3/2}$ and P $2p_{1/2}$ in Co-P, respectively. The high-resolution O 1s (Fig. 4f) spectrum of the 3DOM $\text{Co}_3\text{O}_4/\text{CoP}$ can be deconvoluted into three peaks located at 529.8, 531 and 532.6 eV, corresponding to the

metal-oxygen bonds, low coordinated oxygen atoms and adsorbed moisture, respectively.[36] The existence of low coordinated oxygen atoms could be related to the formation of O-Co-P coordination in the 3DOM $\text{Co}_3\text{O}_4/\text{CoP}$. TGA (Fig. 4g) is used to evaluate the content of sulfur in the as-prepared cathode materials. The sulfur content in the S- $\text{Co}_3\text{O}_4/\text{CoP}$ is proved to be 73%. In comparison with S-CoP cathodes, there is a slight increase of the evaporation temperature observed in S- $\text{Co}_3\text{O}_4/\text{CoP}$, resulting from the significant improved sulfur confinement of the 3DOM $\text{Co}_3\text{O}_4/\text{CoP}$.

Furthermore, the local structure and electronic state effect of Co have been investigated by X-ray absorption near edge structure spectroscopy (XANES), and the extended X-ray absorption fine structure spectroscopy (EXAFS). Obviously, the Co K-edge XANES spectra of 3DOM $\text{Co}_3\text{O}_4/\text{CoP}$ shows a moderate absorption energy (E_0), which is higher than CoP but lower than Co_3O_4 (Fig. 4h) and it exhibits a higher whiteline intensity than that of 3DOM CoP, confirming the formation of 3DOM $\text{Co}_3\text{O}_4/\text{CoP}$ heterostructured materials. The coordination environment of the Co atom is investigated by the FT of EXAFS spectra at the Co K-edge (Fig. 4i). The 3DOM Co_3O_4 FT curve exhibits peaks with a radial distance of 1.50 and 2.48 Å, which can be attributed to Co-O and Co-Co coordination,[37] respectively. In addition, 3DOM CoP shows a major peak at 1.89 Å, which can be assigned to the Co-P peak. Notably, this peak in 3DOM $\text{Co}_3\text{O}_4/\text{CoP}$ undergoes negative shifts to 1.78 Å with a decreased peak intensity, which could be related to the formation of unsaturated coordinated Co on the heterointerface. Therefore, the structural analyzation confirms the formation of heterostructured 3DOM $\text{Co}_3\text{O}_4/\text{CoP}$, which is capable of realizing fast and reliable

Li/S electrocatalytic behavior.

The LiPSs adsorption ability of 3DOM Co₃O₄, 3DOM CoP, and 3DOM Co₃O₄/CoP were further revealed. 10 mg above samples were immersed 5 mM Li₂S₆ solutions in DOL/DME (1.5 mL, v/v = 1:1) for 6 h to examine its color change. The Li₂S₆ solution mixed with the 3DOM Co₃O₄/CoP completely decolorized after adsorption while the solution mixed with 3DOM CoP still demonstrates light yellow color (Inset of Fig. 5a). Such a visual comparison confirms that the 3DOM Co₃O₄/CoP inherits strong adsorption ability from 3DOM Co₃O₄. The supernatant solution was further collected for UV-vis measurement to further quantify the Li₂S₆ adsorption capabilities. The intensity of S₆²⁻ peak at 265 nm in the UV-vis spectrum can be used to calculate the amount of Li₂S₆ remaining in the electrolyte.[38] The solution soaked with the 3DOM Co₃O₄/CoP shows much weaker polysulfide characteristic peaks compared with that of the original Li₂S₆, 3DOM CoP and 3DOM Co₃O₄ (Fig. 5a), demonstrating the strongest LiPSs adsorption capability of the 3DOM Co₃O₄/CoP.

As illustrated in Fig. 5b, the CV curves of assembled symmetric cells obviously reveal a pair of reversible redox peaks. Among these compounds, 3DOM Co₃O₄/CoP presents the minimal polarization for the LiPSs redox transformation, exhibiting excellent electrochemical reversibility and fast LiPSs catalytic conversion kinetics. Besides, the EIS of the 3DOM Co₃O₄/CoP symmetric cell also presents the minimal charge transfer resistance according to semicircle size at high frequency part in the Nyquist plot (Fig. 5c), which exhibits its superior conductivity of 3DOM Co₃O₄/CoP.

The LSV curves are further performed in a three-electrode setup to explore the Li_2S oxidation behavior. As shown in Fig. 5d, the 3DOM $\text{Co}_3\text{O}_4/\text{CoP}$ displays the lowest onset potential of -0.43 V (-0.22, -0.34 V for 3DOM Co_3O_4 and 3DOM CoP, respectively) and higher current response at 5 mV s^{-1} scan rate, demonstrating the lowest energy barrier for the Li_2S oxidation as well as its remarkable catalytic activity. The corresponding Tafel curves of these materials are further revealed in Fig. 5e. Notably, 3DOM $\text{Co}_3\text{O}_4/\text{CoP}$ delivers the lowest Tafel slope of 141 mV dec^{-1} , which is much lower than that of 3DOM Co_3O_4 (166 mV dec^{-1}) and 3DOM CoP (155 mV dec^{-1}), indicating it's the highest reaction kinetics.[39] The fast adsorption-diffusion-conversion process of LiPSs on 3DOM $\text{Co}_3\text{O}_4/\text{CoP}$ is further studied via Li_2S nucleation/precipitation experiment. Clearly, the Li_2S precipitation capacity on 3DOM $\text{Co}_3\text{O}_4/\text{CoP}$ (121 mAh g^{-1}) in Fig. 5f is greatly promoted compared with 3DOM Co_3O_4 (81 mAh g^{-1}) and 3DOM CoP (105 mAh g^{-1}) (Fig. S7). These results distinctly illustrate that the 3DOM $\text{Co}_3\text{O}_4/\text{CoP}$ heterostructured material conspicuously boosts the Li_2S nucleation/precipitation process, resulting in fast LiPSs conversion kinetics.[40, 41]

The Li^+ diffusion coefficient of S- $\text{Co}_3\text{O}_4/\text{CoP}$, S- Co_3O_4 , and S-CoP cathodes were also obtained, as shown in Fig. S8. The S- $\text{Co}_3\text{O}_4/\text{CoP}$ cathode still presents the complete and obvious redox peaks with the increase of scanning rates as well as the highest current value (Fig. S8a-c). The linear relationship obtained by the Randles-Sevcik formula indicates that the slope of peak current (I_p) in relation with the square root of the scan rate $v^{-0.5}$, suggesting a strong diffusion-controlled feature of

electrochemical conversion (Fig. S8d-f).[42] The conversion of LiPSs on the S-Co₃O₄/CoP electrode exhibits the steepest slope, further demonstrating that 3DOM Co₃O₄/CoP can promote the rapid adsorption-diffusion-conversion process for accelerated redox reaction kinetics.[31]

The electrochemical performance of S-Co₃O₄, S-CoP and S-Co₃O₄/CoP composites were further evaluated by assembling three composites in coin cell. According to the CV curves of the sulfur cathodes (Fig. 6a), two cathodic peaks located at approximately 2.32 and 2.06 V can be assigned to the phase transitions from S₈ to high-order Li₂S_x and further reduction into Li₂S₂/Li₂S, respectively. The anodic peak located at ca. 2.40 V is due to short-chain LiPSs are oxidized to long-chain LiPSs and ultimately to S₈. [43, 44] The relatively low polarization value between the cathodic and anodic peak can be obtained in the S-Co₃O₄/CoP electrode, highlighting the higher electrical conductivity, Li/ion conductivity and accelerated insulation Li₂S₂/LiS conversion of S-Co₃O₄/CoP electrode. Fig. 6b depicts the charge/discharge profiles of S-Co₃O₄/CoP cathodes at 0.1 C-rate. The galvanostatic charge-discharge curves clearly present discharge plateaus, consisted with the above CV plots. Specifically, the entire discharging process (Fig S9a) is consisted of upper plateau at stage I (S₈ reduce to Li₂S₈/Li₂S₆) and stage II (subsequently reduce to Li₂S₄) as well as lower plateau at stage III (Li₂S₄ reduce to Li₂S₂/Li₂S). The voltage plateaus remain stable and overlapped even though 100 cycling, indicating its high electrochemical reversibility, confirming its efficiently inhibited LiPSs dissolution and shuttle effect. The charging/discharging profiles of different electrodes are compared

in Fig. S9b. The S-Co₃O₄/CoP electrode delivers a discharge capacity of 1006 mAh g⁻¹ and 532 mAh g⁻¹ at lower and upper plateau, respectively, which is higher than S-Co₃O₄ electrode (986 and 520 mAh g⁻¹, respectively) and S-CoP electrode (719 and 480 mAh g⁻¹, respectively). In addition, the S-Co₃O₄/CoP electrode shows the lowest voltage hysteresis (ΔE) in the Fig. S9b, implying facile electrochemical kinetics and the suppressed LiPSs shuttling behavior. Interestingly, the S-Co₃O₄/CoP electrode depicts the moderate over-potential (2.30 V) and onset potential (1.99 V) during charging (Fig. S9c), which is in line with DFT calculations and yields the fast Li₂S decomposition.[45, 46] These results illustrate that S-Co₃O₄/CoP could improve the sulfur reduction reaction. The rate capability of three electrodes can also be observed in Fig. 6c. The S-Co₃O₄/CoP cathode shows a remarkably steady discharge capacity of 1597 mAh g⁻¹ at 0.1 C (1 C=1675 mA g⁻¹). Meanwhile, along with current density increasing, S-Co₃O₄/CoP cathode still keeps a high discharge capacity of 610 mAh g⁻¹ under 3 C and maintains a decent capacity of 1308 mAh g⁻¹ when the C-rate switched back to 0.1 C, which outperforms than that of S-Co₃O₄ and S-CoP cathodes. Two typical discharge plateaus of S-Co₃O₄/CoP cathode clearly visible even at 3 C, suggesting alleviated polarization (Fig. S10). These results fully demonstrate that the S-Co₃O₄/CoP cathode provides superior rate capability attributed to its stupendous redox reaction kinetics.

The cyclic stability of S-Co₃O₄/CoP, S-Co₃O₄, and S-CoP electrodes are also examined under 0.1 C, as shown in Fig. 6d. Clearly, S-Co₃O₄/CoP presents a highly reversible capacity at 1197 mAh g⁻¹ even after continuous 100 cycles, indicating its

decent capacity retention of 77.8%. In contrast, S-Co₃O₄ and S-CoP cathodes only attain a relatively low capacity of 731 and 455 mAh g⁻¹, respectively, revealing their low capacity retention of 50.6% and 37.9%, respectively. The conversion reaction capacity of 3DOM Co₃O₄/CoP is also evaluated, as shown in Fig. S11. It is clear to see that the electrochemical capacity contribution derived from 3DOM Co₃O₄/CoP can be ignored. Thus, the higher discharge capacity and enhanced cycle stability of S-Co₃O₄/CoP could be related to its strengthened LiPSs adsorption and fast LiPSs conversion of the 3DOM Co₃O₄/CoP. Meanwhile, it can be seen that the S-Co₃O₄/CoP still remains its 3DOM morphology and intact architecture after 100th charging/discharging process, indicating its excellent structural stability (Fig. S12). Furthermore, the long-term cycling stability of the S-Co₃O₄/CoP, S-Co₃O₄ and S-CoP cathodes are further studied (Fig. 6e). After 500 cycles, an admirable reversible capacity of 665 mAh g⁻¹ can be obtained in S-Co₃O₄/CoP cathode with a high average Coulombic efficiency close 100%, corresponding to a remarkably low capacity fading rate of 0.033% per cycle. This superior cyclic stability demonstrates an inhibitory shuttle effect and promoted cycling stability in S-Co₃O₄/CoP attributed to its greatly improved structural stability and efficient adsorption-diffusion-conversion process on the heterointerface.

The electrochemical performance under raised sulfur loading and decreased E/S ratio is critical for practically viable Li/S batteries [47]. To examine its performance practically relevant condition, the composites electrodes with higher areal loading and limited E/S ratio were evaluated. Clearly, the charge/discharge profiles (Fig. 6f) of the

S-Co₃O₄/CoP electrode with two-plateau is well maintained under different sulfur loadings, indicating its favorable redox reaction process. As shown in Fig. 6g, a stable discharge capacity is achieved at different rates for the sulfur loadings of 3.4, 5.3 and 6.4 mg cm⁻² with the corresponding E/S ratio of 8.8, 5.6 and 4.7 mL g⁻¹. Fig. 6h depicts the cyclability of the S-Co₃O₄/CoP electrode, which reflects an initial high specific capacity of 1113, 905 and 757 mAh g⁻¹ at different sulfur loadings. Specifically, after 100 cycles under 0.1 C, S-Co₃O₄/CoP electrode still delivers discharge capacity of 1048, 835 and 688 mAh g⁻¹, respectively. The cycled separator and Li foil of S-Co₃O₄/CoP electrode are shown after 100 cycles in Fig. S13 (0.1 C, 6.4 mg cm⁻²). The cycled separator shows less color and wetting state compared with pristine separator. In addition, the uniform SEI film without obvious dendrite growth, revealing that the Co₃O₄/CoP effectively depresses LiPSs dissolution, electrolyte depletion and lithium corrosion. Nevertheless, the rough Li surface still existence, which need further improve by Li metal protection. Also, two Li/S batteries based on S-Co₃O₄/CoP (Fig. S14) cathode is capable of lighting up a yellow light-emitting diode (LED) lamp plate, disclosing such host material can be used as commercial energy storage systems.

4. Conclusions

In summary, 3DOM TMOs/TMPs heterostructured material is successfully developed and its interfacial redox reaction kinetics in Li/S batteries was fully investigated by adjusting the electronic structures. Benefiting from the decreased energy gap between p and d-bands centers and the reduced energy barrier for LiPSs

diffusion and decomposition on the heterointerface, the 3DOM TMOs/TMPs multifunctional sulfur host presents smooth immobilization-diffusion-conversion process of LiPSs. Meanwhile, the 3DOM TMOs/TMPs offers large surface area and exposes numerous active sites for favored redox reactions while the porous hollow structure is able to homogenize sulfur distribution and provide potent sulfur confinement. This effective design and illumination of 3DOM TMOs/TMPs heterointerfaces will not only guide the sulfur host material design towards fast electrocatalytic behavior, but also enlighten the energy band engineering to understand essential mechanism of defect, heterojunction, and doping system.

Acknowledgments

This work was supported by the Program for the Outstanding Young Talents of Hebei Province, China (Y.G.Z.); Chunhui Project of Ministry of Education of the People's Republic of China (Grant No. Z2017010); Xijiang R&D Team (X.W.); Guangdong Innovative and Entrepreneurial Team Program (No. 2016ZT06C517); Science and Technology Program of Guangzhou (No. 2019050001); Science and Technology Program of Zhaoqing (No. 2019K038); Natural Sciences and Engineering Research Council of Canada, University of Waterloo, and Waterloo Institute for Nanotechnology. The authors also thank the XAS characterizations in BioXAS-side (07ID-2) beamline in Canadian Light Sources.

References

- [1] Y. Ansari, S. Zhang, B.H. Wen, F. Fan, Y.M. Chiang, *Adv. Energy Mater.* 9 (2019) 1802213.
- [2] H. Al Salem, G. BaBu, C.V. Rao, L.M.R. Arava, *J. Am. Chem. Soc.* 137 (2015) 11542-11545.
- [3] J.-H. Kim, Y.-H. Lee, S.-J. Cho, J.-G. Gwon, H.-J. Cho, M. Jang, S.-Y. Lee, S.-Y. Lee, *Energy Environ. Sci.* 12 (2019) 177-186.
- [4] Y. Tian, G.R. Li, Y.G. Zhang, D. Luo, X. Wang, Y. Zhao, H. Liu, P.G. Ji, X.H. Du, J.D. Li, Z.W. Chen, *Adv. Mater.* 32 (2020) 1904876.
- [5] N. Kang, Y.X. Lin, L. Yang, D.P. Lu, J. Xiao, Y. Qi, M. Cai, *Nat. Commun.* 10

- (2019) 4597.
- [6] Y.X. Ren, L. Zeng, H.R. Jiang, W.Q. Ruan, Q. Chen, T.S. Zhao, *Nat. Commun.* 10 (2019) 3249.
- [7] Z.S. Yu, M.L. Liu, D.Y. Guo, J.H. Wang, X. Chen, J. Li, H.L. Jin, Z. Yang, X.A. Chen, S. Wang, *Angew. Chem. Int. Ed.* 59 (2020) 6406-6411.
- [8] G.Q. Tan, R. Xu, Z.Y. Xing, Y.F. Yuan, J. Lu, J.G. Wen, C. Liu, L. Ma, C. Zhan, Q. Liu, T.P. Wu, Z.L. Jian, R. Shahbazian-Yassar, Y. Ren, D.J. Miller, L.A. Curtiss, X.L. Ji, K. Amine, *Nat. Energy* 2 (2017).
- [9] R. Chulliyote, H. Hareendrakrishnakumar, M.G. Joseph, *ACS Sustainable Chem. Eng.* 7 (2019) 19344-19355.
- [10] J.C. Ren, Y.L. Huang, H. Zhu, B.H. Zhang, H.K. Zhu, S.H. Shen, G.Q. Tan, F. Wu, H. He, S. Lan, X.H. Xia, Q. Liu, *Carbon Energy* 2 (2020) 176-202.
- [11] X.L. Ji, K.T. Lee, L.F. Nazar, *Nat. Mater.* 8 (2009) 500-506.
- [12] Q.H.Q. Xiao, G.R. Li, M.J. Li, R.P. Liu, H.B. Li, P.F. Ren, Y. Dong, M. Feng, Z.W. Chen, *J. Energy Chem.* 44 (2020) 61-67.
- [13] Y. Boyjoo, H.D. Shi, E. Olsson, Q. Cai, Z.S. Wu, J. Liu, G.Q. Lu, *Adv. Energy Mater.* (2020) 2000651.
- [14] D. Gueon, J.T. Hwang, S.B. Yang, E. Cho, K. Sohn, D.K. Yang, J.H. Moon, *ACS Nano* 12 (2018) 226-233.
- [15] A. Abdul Razzaq, Y.Z. Yao, R. Shah, P.W. Qi, L.X. Miao, M.Z. Chen, X.H. Zhao, Y. Peng, Z. Deng, *Energy Storage Mater.* 16 (2019) 194-202.
- [16] S. Kim, M. Cho, Y. Lee, *Adv. Funct. Mater.* 30 (2020) 1907680.
- [17] J.R. He, L. Luo, Y.F. Chen, A. Manthiram, *Adv. Mater.* 29 (2017) 1702707.
- [18] X. Liu, J.Q. Huang, Q. Zhang, L.Q. Mai, *Adv. Mater.* 29 (2017) 1601759.
- [19] D. Luo, Z. Zhang, G.R. Li, S.B. Cheng, S. Li, J.D. Li, R. Gao, M. Li, S. Sy, Y.P. Deng, Y. Jiang, Y.F. Zhu, H.Z. Dou, Y.F. Hu, A.P. Yu, Z.W. Chen, *ACS Nano* 14 (2020) 4849-4860.
- [20] D. Luo, G.R. Li, Y.P. Deng, Z. Zhang, J.D. Li, R.L. Liang, M. Li, Y. Jiang, W.W. Zhang, Y.S. Liu, W. Lei, A.P. Yu, Z.W. Chen, *Adv. Energy Mater.* 9 (2019) 1900228.
- [21] J.D. Shen, X.J. Xu, J. Liu, Z.B. Liu, F.K. Li, R.Z. Hu, J.W. Liu, X.H. Hou, Y.Z. Feng, Y. Yu, M. Zhu, *ACS Nano* 13 (2019) 8986-8996.
- [22] H.D. Yuan, X.L. Chen, G.M. Zhou, W.K. Zhang, J.M. Luo, H. Huang, Y.P. Gan, C. Liang, Y. Xia, J. Zhang, J.G. Wang, X.Y. Tao, *ACS Energy Lett.* 2 (2017) 1711-1719.
- [23] T.H. Zhou, W. Lv, J. Li, G.M. Zhou, Y. Zhao, S.X. Fan, B.L. Liu, B.H. Li, F.Y. Kang, Q.H. Yang, *Energy Environ. Sci.* 10 (2017) 1694-1703.
- [24] D.H. Liu, C. Zhang, G.M. Zhou, W. Lv, G.W. Ling, L.J. Zhi, Q.H. Yang, *Adv. Sci.* 5 (2018) 1700270.
- [25] Z.H. Shen, M.Q. Cao, Z.L. Zhang, J. Pu, C.L. Zhong, J.C. Li, H.X. Ma, F.J. Li, J. Zhu, F. Pan, H.G. Zhang, *Adv. Funct. Mater.* (2019) 1906661.
- [26] Z. Shen, Z. Zhang, M. Li, Y. Yuan, Y. Zhao, S. Zhang, C. Zhong, J. Zhu, J. Lu, H. Zhang, *ACS Nano* (2020).
- [27] W. Fan, M.A. Snyder, S. Kumar, P.S. Lee, W.C. Yoo, A.V. McCormick, R. Lee Penn, A. Stein, M. Tsapatsis, *Nat. Mater.* 7 (2008) 984-991.

- [28] K. Chen, X.J. Wang, G. Wang, B.B. Wang, X.J. Liu, J.T. Bai, H. Wang, *Chem. Eng. J.* 347 (2018) 552-562.
- [29] Y. Zheng, T.F. Zhou, C.F. Zhang, J.F. Mao, H.K. Liu, Z.P. Guo, *Angew. Chem. Int. Ed. Engl.* 55 (2016) 3408-3413.
- [30] L. Cao, X.W. Gao, B. Zhang, X. Ou, J.F. Zhang, W.B. Luo, *ACS Nano* 14 (2020) 3610-3620.
- [31] Z.X. Cao, J.Y. Jia, S.N. Chen, H.H. Li, M. Sang, M.G. Yang, X.X. Wang, S. Yang, *ACS Appl. Mater. Interfaces* 11 (2019) 39772-39781.
- [32] M.L. Wang, Y.Z. Song, Z.T. Sun, Y.L. Shao, C.W. Wei, Z. Xia, Z.N. Tian, Z.F. Liu, J.Y. Sun, *ACS Nano* 13 (2019) 13235-13243.
- [33] R.R. Li, X.J. Zhou, H.J. Shen, M.H. Yang, C.L. Li, *ACS Nano* 13 (2019) 10049-10061.
- [34] T. Liu, L.Y. Zhang, W. You, J.G. Yu, *Small* 14 (2018) 1702407.
- [35] M.M. Guo, Y.H. Qu, C.L. Yuan, S. Chen, *Electrochim. Acta* 322 (2019) 134768.
- [36] J.k. Wang, R. Gao, L.R. Zheng, Z.J. Chen, Z.H. Wu, L.M. Sun, Z.B. Hu, X.F. Liu, *ACS Catal.* 8 (2018) 8953-8960.
- [37] Y. Sa, K. Kwon, J. Cheon, F. Kleitz, S. Joo, *J. Mater. Chem. A* 1 (2013) 9992-10001.
- [38] J. Tan, D.N. Liu, X. Xu, L.Q. Mai, *Nanoscale* 9 (2017) 19001-19016.
- [39] M. Zhao, H.J. Peng, Z.W. Zhang, B.Q. Li, X. Chen, J. Xie, X. Chen, J.Y. Wei, Q. Zhang, J.Q. Huang, *Angew. Chem. Int. Ed. Engl.* 58 (2019) 3779-3783.
- [40] Z.L. Xu, S.H. Lin, N. Onofrio, L.M. Zhou, F.Y. Shi, W. Lu, K. Kang, Q. Zhang, S.P. Lau, *Nat. Commun.* 9 (2018) 4164.
- [41] B.-Q. Li, H.-J. Peng, X. Chen, S.-Y. Zhang, J. Xie, C.-X. Zhao, Q. Zhang, *CCS Chem.* (2019) 128-137.
- [42] G.I. Cui, G.R. Li, D. Luo, Y.G. Zhang, Y. Zhao, D.R. Wang, J.Y. Wang, Z. Zhang, X. Wang, Z.W. Chen, *Nano Energy* 72 (2020) 104685.
- [43] L.L. Xu, H.Y. Zhao, M.Z. Sun, B.L. Huang, J.W. Wang, J.L. Xia, N. Li, D.D. Yin, M. Luo, F. Luo, Y.P. Du, C.H. Yan, *Angew. Chem. Int. Ed. Engl.* 58 (2019) 11491-11496.
- [44] Z.S. Wang, J.D. Shen, J. Liu, X.J. Xu, Z.B. Liu, R.Z. Hu, L.C. Yang, Y.Z. Feng, J. Liu, Z.C. Shi, L. Ouyang, Y. Yu, M. Zhu, *Adv. Mater.* 31 (2019) 1902228.
- [45] K. Lu, H. Zhang, S.Y. Gao, H.Y. Ma, J.Z. Chen, Y.W. Cheng, *Adv. Funct. Mater.* 29 (2019) 1807309.
- [46] Z. Ye, Y. Jiang, L. Li, F. Wu, R. Chen, *Adv. Mater.* 32 (2020) e2002168.
- [47] Z.-W. Zhang, H.-J. Peng, M. Zhao, J.-Q. Huang, *Adv. Funct. Mater.* 28 (2018) 1707536.

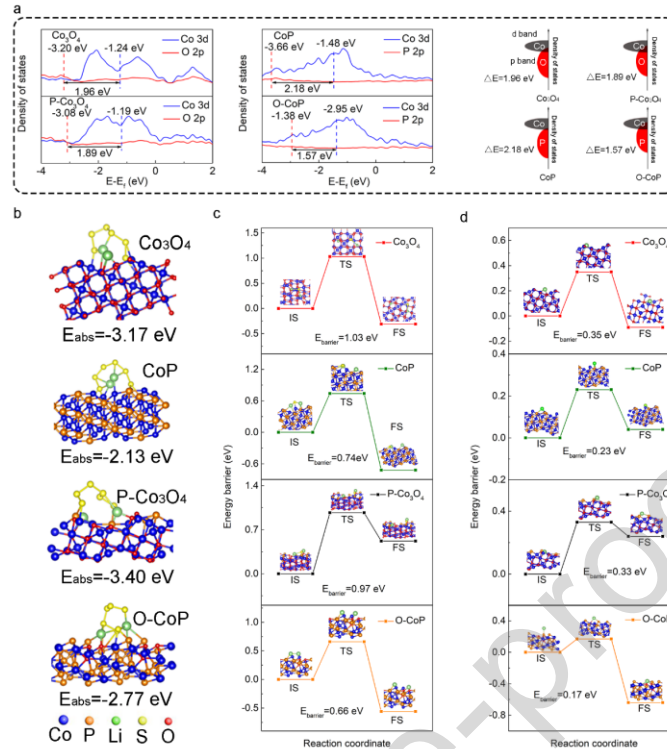


Fig. 1. Mechanism illumination of fast LiPSs catalytic effect on TMOs/TMPs: (a) density of states of Co₃O₄, P-Co₃O₄, CoP and O-CoP; (b) first-principles calculations of absorption energy between Li₂S₆ and Co₃O₄, CoP, P-Co₃O₄ and O-CoP surface; (c) energy barrier of Li₂S decomposition on Co₃O₄, CoP, P-Co₃O₄ and O-CoP surface; (d) Li⁺ diffusion energy barrier on Co₃O₄, CoP, P-Co₃O₄ and O-CoP surface.

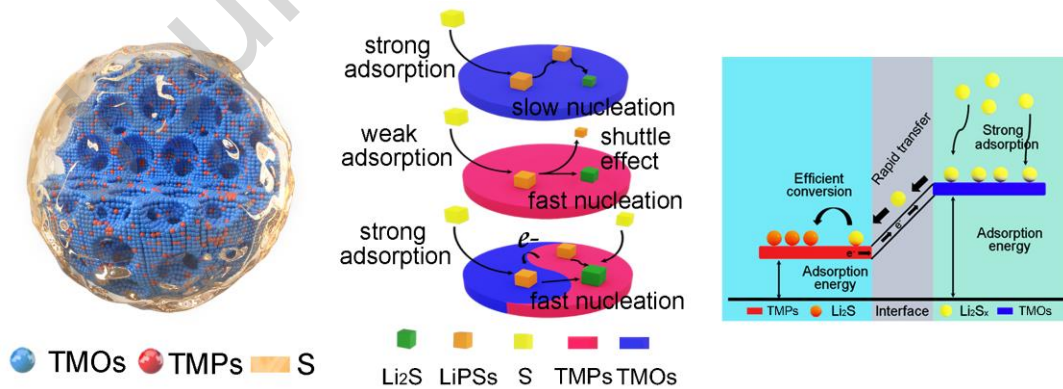


Fig. 2. Schematics of LiPSs species conversion and Li₂S nucleation process on the 3DOM TMOs, 3DOM TMPs and 3DOM TMOs/TMPs.

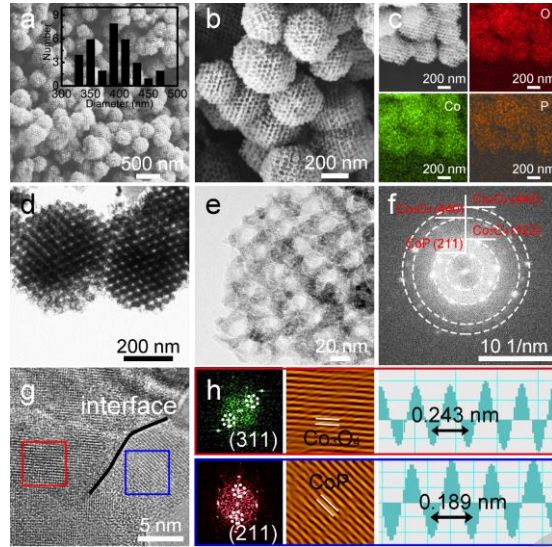


Fig. 3. Morphological analysis of the 3DOM $\text{Co}_3\text{O}_4/\text{CoP}$: (a, b) SEM images and corresponding (c) elemental mapping of the 3DOM $\text{Co}_3\text{O}_4/\text{CoP}$; (d, e) TEM images, (f) SAED pattern, (g) HRTEM image and (h) corresponding fast Fourier transform images of the 3DOM $\text{Co}_3\text{O}_4/\text{CoP}$. Inset of (a): Histograms of size 3DOM $\text{Co}_3\text{O}_4/\text{CoP}$ nanospheres.

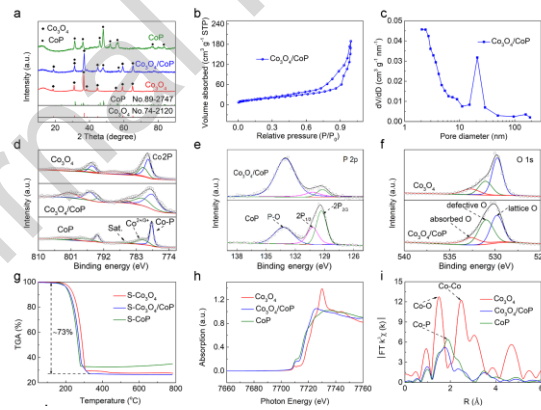


Fig. 4. Structural evaluation of the 3DOM $\text{Co}_3\text{O}_4/\text{CoP}$: (a) XRD patterns of the 3DOM $\text{Co}_3\text{O}_4/\text{CoP}$, 3DOM Co_3O_4 , and 3DOM CoP ; (b) nitrogen adsorption/desorption isotherms and (c) PSD of the 3DOM $\text{Co}_3\text{O}_4/\text{CoP}$; XPS spectra of the 3DOM $\text{Co}_3\text{O}_4/\text{CoP}$: (d) Co 2p, (e) P 2p, and (f) O 1s; (g) TGA profiles of the S- $\text{Co}_3\text{O}_4/\text{CoP}$, S- Co_3O_4 , and S- CoP ; (h) Co K-edge XANES spectra of the 3DOM $\text{Co}_3\text{O}_4/\text{CoP}$, 3DOM Co_3O_4 and 3DOM CoP ; (i) corresponding Fourier transform k^3 -weighted $\chi(k)$ -function of the EXAFS spectra of the 3DOM $\text{Co}_3\text{O}_4/\text{CoP}$, 3DOM Co_3O_4 , and 3DOM CoP .

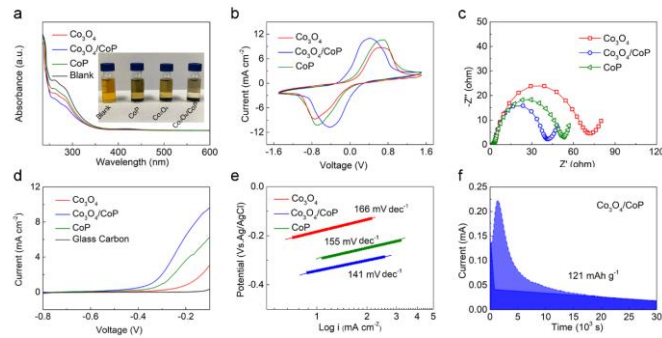


Fig. 5. LiPSs adsorption and catalytic conversion evaluation on different sulfur host: (a) UV-vis spectra and the visualized Li_2S_6 solutions adsorbed by the 3DOM $\text{Co}_3\text{O}_4/\text{CoP}$, 3DOM Co_3O_4 , and 3DOM CoP ; (b) CV curves of symmetric cells; (c) EIS of symmetric cells; (d) LSV curves; (e) Tafel curves of Li_2S oxidation for three electrodes and (f) Li_2S deposition profiles for 3DOM $\text{Co}_3\text{O}_4/\text{CoP}$ electrodes.

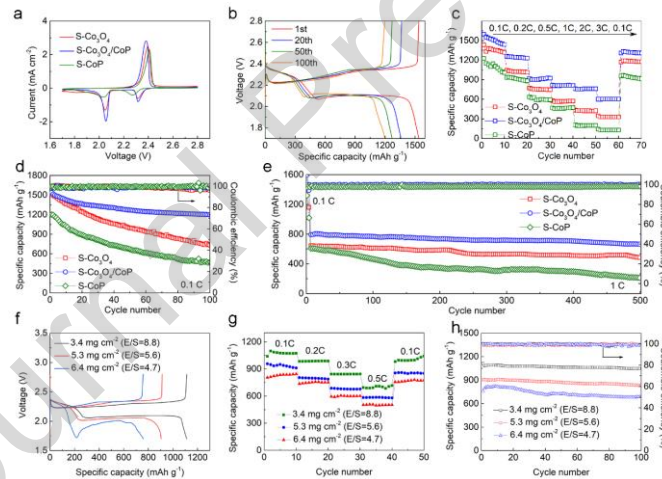


Fig. 6. Electrochemical performance of S- $\text{Co}_3\text{O}_4/\text{CoP}$, S- Co_3O_4 , and S- CoP cathode: (a) CV curves; (b) charge/discharge curves at different cycles; (c) rate performance; (d) cycling performance at 0.1 C; (e) long-term cycling performance at 1 C; Electrochemical performance of S- $\text{Co}_3\text{O}_4/\text{CoP}$ electrodes under raised sulfur loadings and limited E/S ratio: (f) charge/discharge profiles; (g) rate performance and (h) cycling performance at 0.1 C.



Daorui Wang received his Master degree in School of Material Science and Engineering from Hebei University of Technology. Now he works in School of Information and Optoelectronic Science and Engineering & International Academy of Optoelectronics at Zhaoqing, South China Normal University, as an engineer. His research focuses on advanced nanomaterials for energy conversion.



Dr. Dan Luo received his Ph.D degree in Chemical Engineering from University of Waterloo and now he is a postdoctoral fellow under the supervision of Prof. Zhongwei Chen at the University of Waterloo. His research focuses on the development of novel electrode materials, structures and electrolyte for rechargeable lithium-sulfur batteries and solid-state lithium batteries.



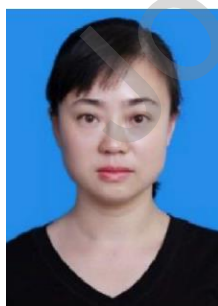
Yongguang Zhang is an Associate Professor of School of Materials Science and Engineering at Hebei University of Technology, China. He received his BS and Master degree in Chemical Engineering from Tianjin University, and earned his Ph.D in Chemical Engineering at University of Waterloo in 2013. His current interests include the synthesis and characterization of nanomaterials for energy storage and conversion, especially for lithium-ion batteries and lithium/sulfur batteries.



Yan Zhao received her Master degree in Chemical Engineering from University of Waterloo. Currently, she is a lab technician at the Hebei University of Technology. Her current research focuses on the nanostructured materials for energy applications.



Prof. Guofu Zhou is a China National Distinguished Professor in the field of micro/nano optoelectronic materials, devices and flat panel displays at South China Normal University (SCNU) and Co-founder & Director of Electronic Paper Display Institute of SCNU, National Center for International Research on Green Optoelectronics and joint research labs of SCNU-TUE, -UT and -UG. He is currently leading several national research projects and Sino-Dutch joint projects. Prof. Zhou is winner of the ISMANAM-1994 Best Young Scientist Gold Medal and Philips “Gilles Holst” Award for the year 2006.



Prof. Lingling Shui received her Ph.D degree in Electrical Engineering from Twente University (2009), the Netherlands. She is now a full professor at South China Academy of Advanced Optoelectronics & School of Information and Optoelectronic Science and Engineering, South China Normal University. Her research interests are fundamentals and applications based on microfluidics and electrofluidic technologies, especially for sensors, actuators and displays.

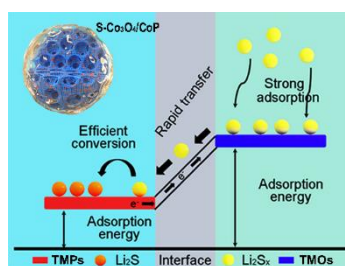


Dr. Zhongwei Chen is Canada Research Chair Professor in Advanced Materials for Clean Energy at the University of Waterloo, the Fellow of the Royal Society of Canada, the Fellow of the Canadian Academy of Engineering and Vice President of International Academy of Electrochemical Energy Science (IAOEES). His research interests are the development of advanced energy materials and electrodes for fuel cells, metal air batteries, and lithium-ion batteries. He has published 2 book, 9 book chapters and more than 300 peer reviewed journal articles with over 28,000 citations with a H-index of 83 (GoogleScholar).



Prof. Xin Wang received his Ph.D degree from Beijing Normal University at 2012. After that, Dr. Wang work in University of Waterloo (Canada) as a postdoc fellow and then he joined South China Normal University (China). He has been working on electrochemistry technology for energy conversion and storage, including electrocatalysis, photocatalysis, Li-ion batteries, Li/S battery and other energy storage materials and devices.

Graphical abstract



The typical reaction mechanism of transition metal oxides/transition metal phosphates (TMOs/TMPs) for Li/S chemistry.

Highlights

1. The three dimensional ordered mesoporous (3DOM) $\text{Co}_3\text{O}_4/\text{CoP}$ heterostructured material is developed as a high-performance Li/S batteries cathode electrocatalyst.
2. The interpenetrated interface of transition metal oxides/phosphates reduced energy gap between the energy centers of the cation 3d and anion 2p bands center to reveal the fast Li/S electrocatalytic behavior of 3DOM $\text{Co}_3\text{O}_4/\text{CoP}$.
3. The obtained S- $\text{Co}_3\text{O}_4/\text{CoP}$ cathode enables outstanding cycling stability and under the limited electrolyte.

Credit author statement

Daorui Wang: Conceptualization, Investigation, Data curation, Writing - original draft. **Dan Luo:** Conceptualization, Writing-review & editing, Supervision. **Yongguang Zhang:** Resources, Conceptualization, Supervision, Writing-review & editing, Project administration, Funding acquisition. **Yan Zhao:** Resources, Conceptualization, Supervision, Writing-review & editing, Project administration, Funding acquisition. **Guofu Zhou:** Resources, Conceptualization, Supervision, Writing-review & editing, Project administration, Funding acquisition. **Lingling Shui:** Resources, Conceptualization, Supervision, Writing-review & editing, Project administration, Funding acquisition. **Zhongwei Chen:** Resources, Conceptualization, Supervision, Writing-review & editing, Project administration, Funding acquisition. **Xin Wang:** Resources, Conceptualization, Supervision, Writing-review & editing, Project administration, Funding acquisition.

Declaration of interests

The authors declare that they have no known competing financial interests or personal relationships that could have appeared to influence the work reported in this paper.

The authors declare the following financial interests/personal relationships which may be considered as potential competing interests:

Journal Pre-proof